NH3 synthesis in a dielectric barrier discharge reactor: a study from atmospheric to low pressure

Rodrigo Antunes, Arne Meindl, Ante Hecimovic, Ursel Fantz

Antunes, Rodrigo, Arne Meindl, Ante Hecimovic, and Ursel Fantz. 2026. "NH3 synthesis in a dielectric barrier discharge reactor: a study from atmospheric to low pressure." *Plasma Chemistry and Plasma Processing* 46 (3): 44. https://doi.org/10.1007/s11090-026-10656-6.

Plasma Chemistry and Plasma Processing (2026) 46:44
https://doi.org/10.1007/s11090-026-10656-6

ORIGINAL PAPER

NH_3 Synthesis in a Dielectric Barrier Discharge Reactor: A Study from Atmospheric to Low Pressure

Rodrigo Antunes[1] · **Arne Meindl**[1] · **Ante Hecimovic**[1] · **Ursel Fantz**[1,2]

Received: 2 December 2025 / Accepted: 17 February 2026

Abstract

N_2-H_2 discharges are systematically studied using a coaxial dielectric barrier discharge reactor for ammonia synthesis by means of mass spectrometry, electrical characterization and high-resolution emission spectroscopy. The influence of packing is investigated by accommodating chemically inert SiO_2 beads in the discharge volume from 920 to 13 mbar. Above 275 mbar, the discharge is dominated by filaments associated with intense microdischarges, whereas at lower pressures, the plasma becomes diffuse and occupies a large volume. In presence of packing, the intensity of the microdischarges at 920 mbar are strongly suppressed, while the electrical and emission properties of the diffuse plasma remain largely unaffected. The absence of intense microdischarges in the diffuse mode at low pressures eliminates important NH_3 dissociation channels. Decreasing the pressure below 100 mbar leads to a significant increase in $[NH_3]$ with SiO_2 beads. This is attributed to both an increase of E/n, which favours H_2 and N_2 dissociation, and consequently to an increase in plasma-surface reactions involving H and N towards ammonia formation. Investigations at 50 mbar reveal that introducing SiO_2 beads in contact with the plasma has a more limited impact on $[NH_3]$ than at 920 mbar. The emission spectra are dominated by the second positive system of N_2, first negative system of N_2^+, and H_α, with no evidence of excited NH^*. The rotational temperature of $N_2(C)$ is mostly affected by $[N_2]$ in $[H_2]$ in the empty reactor at 920 mbar, reaching about 808 K at 75 vol.% N_2. With packing or at 50 mbar the rotational temperature remains at $\approx 400\,\mathrm{K}$. For all tested conditions, the vibrational temperatures of $N_2(C)$ lie in the range of $3500 - 3900\,\mathrm{K}$.

Keywords DBD · ammonia synthesis · pressure · spectroscopy

✉ Rodrigo Antunes
rodrigo.antunes@ipp.mpg.de

[1] Max Planck Institute for Plasma Physics, Boltzmannstrasse 2, 85748 Garching b. München, Germany

[2] AG Experimentelle Plasmaphysik, University of Augsburg, 86135 Augsburg, Germany

Introduction

Several plasma sources have been studied for the synthesis of ammonia (NH_3) using nitrogen-hydrogen (N_2-H_2) mixtures, which include low pressure plasmas, such as microwave [1, 2], radiofrequency (RF) [3, 4] or glow discharges [5, 6], and atmospheric pressure plasmas, such as Dielectric Barrier Discharges (DBDs) [7, 8] or RF discharges [9]. For all plasmas, NH_3 synthesis is possible by generating a discharge containing H_2 and N_2 without any catalyst at pressures and gas temperatures significantly lower than those in the commercial Haber-Bosch process, which relies on a reactor packed with an iron-based catalyst operated at $100-200\,\mathrm{bar}$ and $723\,\mathrm{K}$ [10]. This is enabled by the highly reactive environment of plasmas. The presence of metallic surfaces [11], dielectric beads [12], conventional catalysts with active phases and promoters [13] or porous zeolites [14] do usually lead to larger formation rates than with plasma alone. For instance, Gorbanev et al. studied the influence of doping Al_2O_3 beads with transition metals on ammonia synthesis using a DBD [8]. Although differences in synthesis rates between iron, ruthenium, cobalt and copper are reported, these differences appear to be minimal when compared to the well-known volcano plot in thermal catalysis. Such a volcano plot was predicted to occur in plasmas as well by Mehta et al., who predicted that the rate-limiting step was the dissociation of vibrationally excited N_2 [15]. However, when extending this model to radical adsorption and Eley-Rideal (E-R) reactions, no volcano plot is retrieved, and a very good match with plasma-catalytic experiments is obtained [8]. Plasma-surface reactions involving radicals such as H, N or NH are identified as key to enable the increased formation rates. Atomic H and N, mainly produced by electron-impact dissociation of H_2 and N_2 in the plasma, can adsorb on the catalyst surface and be involved in hydrogenation of N(s) towards NH_3 by Eley-Rideal and Langmuir-Hinshelwood reactions. The formation of NH_x(s) on a metallic surface through E-R reactions has been experimentally demonstrated [16]. Numerical studies have suggested that the dissociation of N_2 into N followed by its adsorption is the rate-limiting step [17]. Bayer et al. demonstrated that in atmospheric RF plasma jets, although the production of vibrationally excited $N_2(\nu)$ exceeds that of atomic N, the relaxation of $N_2(\nu)$ on the catalyst surface makes its contribution to the formation of NH_3 significantly less important than that of N [18]. Electron-impact dissociation of NH_3 has been identified to be the main loss channel in various plasmas [19–21], one example of which being the NH_3 dissociation taking place in microdischarges in DBDs. Other works have identified additional channels such as collisions between NH_3 and atomic N(^{2}D), N_2H^+ or excited $N_2(A^3)$ [22, 23], while thermal decomposition of NH_3 is the main destruction mechanism in warm and thermal plasmas [24, 25].

Owing to their relative ease of operation at atmospheric pressure and compatibility with catalytic surfaces due to relatively low gas temperatures, DBDs are by far the most studied plasmas for ammonia synthesis. DBDs operate at comparatively large *E*/*n*, often in the order of hundreds of Td, which favour the production of electronically excited species and radicals [26]. In general, studies are focussed on how ammonia yields are affected by macroscopically accessible parameters, such as discharge power, flow rates or gas inlet composition in presence of a wide variety of packing materials. Both physical and chemical properties of the packing materials influence the resulting plasma electrical characteristics and chemistry, making it challenging in many studies to disentangle their individual effects [13]. For instance, De Meyer et al. systematically studied how the packing of a DBD reactor with γ-Al_2O_3 beads with and without metallic doping can affect the morphology and electrical characteristics of N_2-H_2 discharges and ammonia formation [27]. The modification of the plasma from filamentary to a homogeneous discharge by spray-coating the beads with cobalt or nickel led to a significant improvement in NH_3 formation. This enhancement is attributed to a large volume occupation and an absence of filaments which contribute to ammonia dissociation by electron-impact dissociation.

Beyond the lack of systematic study of the electrical properties of DBD discharges in the literature of plasma-catalysis [28], the use of spectroscopic tools such as high-resolution optical emission spectroscopy (OES) to gain insights into the plasma chemistry remains limited. Great focus is usually given to NH^* (with most intense peak at 336.0 nm), which indicates the presence of a key ammonia precursor in the plasma volume [7, 14, 29]. However, its emission strongly overlaps with that of the main N_2^* band ($334 - 337.1$ nm), which hinders its identification with widely used low-resolution spectrometers. By means of high-resolution spectroscopy, Chen et al. did not observe NH^* under various conditions of plasma power in a packed DBD [30], thereby highlighting the need for further systematic studies.

This work aims at providing a systematic study of N_2-H_2 discharges for the formation of ammonia in a coaxial DBD reactor by means of mass spectrometry (MS), electrical characterization and high-resolution OES. The investigations are carried out with the reactor in an empty configuration as well as packed with SiO_2 beads. The choice of packing material is not aimed at maximizing performances, but rather to exclude the influence of any potential chemical (catalytic) effect on the plasma properties. In particular, this work demonstrates the influence of packing a DBD discharge on important plasma parameters, such as the vibrational and rotational temperatures of $N_2(C)$ and chemistry of the excited states in N_2-H_2 plasmas, which are often not reported in the literature of ammonia synthesis with DBDs. This study also investigates the role of pressure, a largely unexplored parameter in the literature of DBDs, on the discharge properties across the range of 920 to 13 mbar.

Experimental

The schematic of the experimental setup used is depicted in Fig. 1. A coaxial DBD reactor features a quartz tube with an inner/outer diameter of 22/25 mm, a 34 mm long, 12.7 mm wide inner stainless steel rod and a stainless steel mesh of equal length tightly wrapped around the outer wall of the quartz tube. The inner electrode is kept in place by two 3.5 mm thick alumina rings placed at both ends and it is connected to the ground via a feedthrough. A monitoring capacitor ($C_\mathrm{m} = 22\,\mathrm{nF}$) is installed between the feedthrough and the ground, and the voltage V_c across it is measured by a passive probe (Teledyne LeCroy, PP026). A current transformer (Magnelab Inc., CT-D1.0-B) is used to measure the total current, while a high-voltage probe (Testec, TT-HVP 2739) measures the applied voltage V_app supplied by a power generator (AFS G05F), operating at a frequency of 23.6 kHz. The applied high-voltage, the voltage across the capacitor and the current waveforms are recorded with an oscilloscope (Teledyne LeCroy, WaveSurfer 4024HD 200 MHz). The discharge is continuously cooled with two pressurized air blowers placed perpendicularly to the quartz tube axis, which guarantees that the temperature changes remain limited and comparable for all conditions investigated in this work. A digital camera (Nikon, Z30) is used to take photos of the discharge. The gases (Air Liquide, purity 5.0 for N_2 and 6.0 for H_2) are supplied to

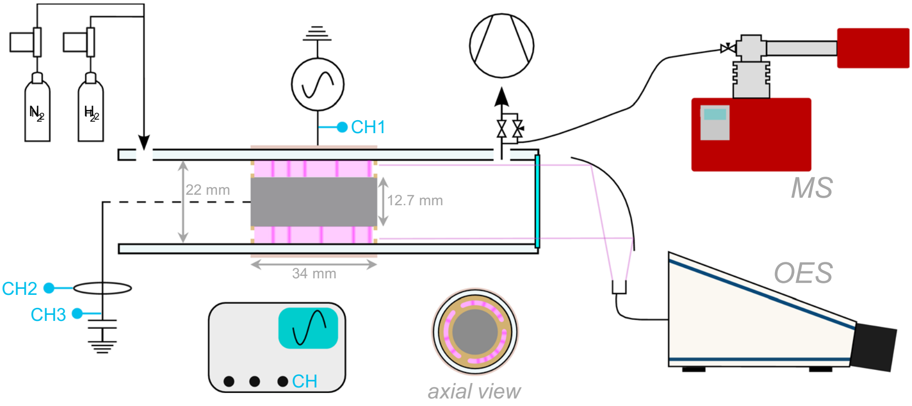

Fig. 1 Experimental setup depicting the co-axial DBD, electrical circuit and dignostics of mass spectrometry and Echelle spectrometer

Table 1 Experimental matrix

Packing	P_{gen} / W	$[N_2]$ / vol.%	F_{total} / sccm	p / mbar
Empty, SiO_2	$40-110$	25	100	920, 50
Empty, SiO_2	100	$10-75$	100	920, 50
Empty, SiO_2	100	25	$25-300$	920, 50
Empty, SiO_2	100	25	100	$13-920$

the reactor by means of mass flow controllers (Brooks Instrument, GF40), and a vacuum pump (Leybold, TRIVAC D16B) connected to the outlet of the reactor enables studying the discharge at different pressures. The pressure in the reactor is regulated by a high-precision dosing valve and its absolute value is measured by a sensor (Pfeiffer Vacuum, CM361) placed upstream of the reactor. A sampling line between the outlet of the reactor and the dosing valve is connected to a quadrupole mass spectrometer (Pfeiffer Vacuum, QMG 220 PrismaPlus) to determine the gas composition. An absolutely calibrated, high-resolution Echelle spectrometer (LTB Berlin, Aryelle 400 with $\lambda/\Delta\lambda = 45000$) is used to acquire the emission spectra of the discharge axially through a quartz window. To prevent contribution from unwanted discharges between the mesh and the quartz wall to the emission spectra, the outer wall of the quartz tube has been painted black, without a measurable impact on the electrical waveforms and ammonia synthesis compared to the unpainted quartz tube. Note that the exposure times of both the digital camera (40 ms) and emission spectrometer ($\sim$ minutes) are significantly larger than the period of the applied voltage ($\sim 40\,\mu$s) and time scales of microdischarges ($\sim 10-100\,$ns), thereby representing a temporal- and spatially-averaged information of the discharge.

Experimental Matrix

H_2–N_2 discharges are studied over a wide range of parameters summarized in Table 1. At 920 mbar and 50 mbar, the generator power P_{gen} is varied between 40 and 110 W, the total volumetric flow rate F_{total} spans 25 to 300 sccm (sccm corresponds to cm^3 min^{-1} at $T_0 = 273.15\,$K and $p_0 = 1013$ mbar) and the feed gas composition ranges from

10 to 75 vol.% N_2. For the reference conditions of $P_{\text{gen}} = 100\,\text{W}$, $F_{\text{total}} = 100\,\text{sccm}$, $[N_2] = 25\,\text{vol.\%}$, the pressure is varied from 920 down to 13 mbar. The latter corresponds to the lowest pressure achieved for a flow rate of 100 sccm. These conditions are carried out for the empty reactor as well as with a packing of $1.4 - 1.8\,\text{mm}$ dense, non-porous SiO_2 beads (Sigmund Lindner GmbH, Typ Q). The packing fraction γ is estimated to be 0.64. Mass spectrometer as well as electrical measurements are carried out simultaneously and the results are discussed in the next sections. OES measurements are done for most of the experimental conditions, with the exception being those where the light intensity emitted by the discharge is too weak (e.g. low powers at 920 mbar). All conditions were repeated at least once and the average values are presented and discussed. The statistical component of the uncertainties are determined with the standard deviation of several measurements, while the systematic component is calculated using the information available from calibrations.

In order to measure bulk gas temperatures during plasma operation, the quartz window used for OES was replaced by a feedthrough with a type K thermocouple, concentrically installed 10 mm downstream of the discharge. For all operating conditions the gas temperature measured by the thermocouple ranged between 320 and 373 K.

Mass Spectrometer

The mass spectrometer has been calibrated for H_2, N_2 and NH_3 following the procedure described in [31], in which gas bottles (Air Liquide) containing calibrated mixtures of around 50 vol.% of the molecule of interest and 50 vol.% argon are used. The presence of residual water H_2O (mass-to-charge ratio, *m/z* = 18) inside the MS chamber influences the NH_3 (*m/z* = 17) current signal upon cracking of H_2O into OH. While a calibration for H_2O is not trivial and was not performed, the cracking pattern of H_2O into OH (*m/z* = 17) could be estimated by allowing a steady release of water from highly porous Al_2O_3. The estimated contribution of H_2O to the current at *m/z* = 17 is subtracted and the resulting value considered to be from ammonia only. Notwithstanding, the H_2O current signal is significantly lower than that of NH_3 and therefore its influence on the final concentrations is minor.

As a typical procedure, the current signals of *m/z* = 17 and *m/z* = 18 are measured before and after plasma and its average is used as background and subtracted from the signals estimated during plasma operation, thereby yielding net currents: $I_{17}^{\text{net}} = I_{17} - BG_{17}$ and $I_{18}^{\text{net}} = I_{18} - BG_{18}$. The signals of the main gas species during plasma, N_2 and H_2, are subtracted from their background values before gas injection. The resulting current values for the species of interest, which are proportional to their molar flow rates, are determined using relations (1)–(4): the denominators represent the calibration factors in respect to argon, while the contributions of NH_3 cracking to *m/z* = 2, 18, 28 and the cracking of H_2O to *m/z* = 17 are given in the numerators. The background without plasma typically reaches constant values within 10 min, while 15 min are usually required for the signals to reach steady-state during discharge.

$$I_{H_2} = \frac{I_2^{\text{net}} - I_{NH_3} \times 0.013}{2.196} \tag{1}$$

$$I_{N_2} = \frac{I_{28}^{\text{net}} - I_{NH_3} \times 0.005}{0.971} \tag{2}$$

$$I_{\mathrm{NH_3}} = \frac{I_{17}^{\mathrm{net}} - I_{\mathrm{H_2O}} \times 0.320}{1.353} \tag{3}$$

$$I_{\mathrm{H_2O}} = \frac{I_{18}^{\mathrm{net}} - I_{17}^{\mathrm{net}} \times 0.010}{1.277} \tag{4}$$

The concentration of ammonia is determined using Eq. (5) and the Specific Energy Input (SEI), which defines the average energy delivered per molecule, is given by relation (6) expressed in $\mathrm{eV\,molec.}^{-1}$ [32]. P_{plasma} is the plasma power determined using the electrical chracteristics as described in the next section and τ_{plasma} is the residence time, defined by the time a molecule is exposed to the plasma and it depends on the gas pressure *p* and temperature *T* inside the reactor (Eq. (7), where $T_0 = 273.15\,\mathrm{K}$ and $p_0 = 1013$ mbar). $N_{\mathrm{plasma}} = nV_{\mathrm{plasma}}(1-\gamma)$ is the number of particles in the discharge volume V_{plasma} with *n* being the gas number density and γ the packing fraction.

For simplicity, a constant $T = 373\,\mathrm{K}$ is used for the residence time and E/*n* calculations. As discussed below, the rotational temperature (T_{rot}) becomes closer to the background gas temperature with the decrease of pressure, while at 920 mbar it is more representative of the plasma filaments and less of the surrounding gas.

$$[\mathrm{NH_3}] = \frac{I_{\mathrm{NH_3}}}{I_{\mathrm{H_2}} + I_{\mathrm{N_2}} + I_{\mathrm{NH_3}} + I_{\mathrm{H_2O}}} \tag{5}$$

$$\mathrm{SEI} = \frac{P_{\mathrm{plasma}}\tau_{\mathrm{plasma}}}{N_{\mathrm{plasma}}} \times 6.24 \times 10^{18}\,\mathrm{eV\,J^{-1}} \simeq 13.9\frac{P_{\mathrm{plasma}}\,[\mathrm{W}]}{F_{\mathrm{total}}\,[\mathrm{sccm}]} \tag{6}$$

$$\tau_{\mathrm{plasma}} = (1-\gamma)\frac{V_{\mathrm{plasma}}}{F_{\mathrm{total}}\left(\frac{p_0}{p}\right)\left(\frac{T}{T_0}\right)} \tag{7}$$

$$N_{\mathrm{plasma}} = nV_{\mathrm{plasma}}(1-\gamma) = \frac{p}{k_{\mathrm{B}}T}V_{\mathrm{plasma}}(1-\gamma) \tag{8}$$

Electrical Characteristics

During plasma operation waveforms encompassing eleven cycles (time spanning $500\,\mu\mathrm{s}$) are saved within regular intervals. For each cycle the electrical energy consumed by the plasma is determined via the widely used Lissajous and current methods. The former is determined by integrating the Lissajous curve (Fig. 2), which plots the total charge Q_{total} transferred over one cycle as a function of the applied voltage V_{app}, while the latter is determined by integrating the product of the total current i_{total} with V_{app}. Q_{total} is determined by the product between the voltage V_{c} across the monitoring capacitor and its capacitance C_{m}. The product of these integrals with the frequency *f* of the applied high-voltage yields the plasma power, which typically reaches stable values within 15 min of plasma operation. Owing to the similar values using both methods, only the Lissajous powers will be presented.

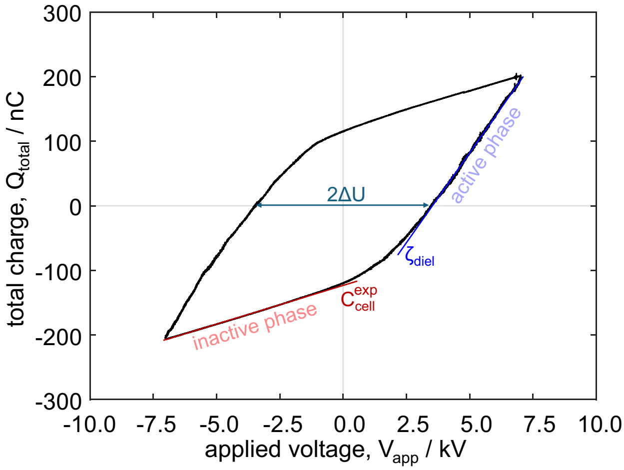

Fig. 2 Example of a Lissajous curve obtained for the reactor packed with SiO_2 beads at 920 mbar with $P_{gen} = 100\,W$, $F_{total} = 100\,sccm$, $[N_2] = 25\,vol.\%$

The Lissajous curves are also used to experimentally determine the cell (C^{exp}_{cell}) and dielectric (ζ_{diel}) capacitances by fitting the slopes of the inactive and active phases with first order polynomials (Fig. 2). C^{exp}_{cell} is the capacitance of the reactor without plasma, while ζ_{diel} assumes a value between zero and the capacitance of the dielectric barrier (C_{diel}) and it can be used to determine the discharge fraction β, defined according to Eq. (9) [33]. As recently discussed by De Meyer et al., the determination of β, which can be used as proxy for the plasma volume, can give important insights into NH_3 formation in DBDs [27]. A partially-bridged gap corresponds to $0 < \beta < 1$, while a discharge completely covering both electrodes yields $\beta = 1$. The uncertainty in the dielectric constant of quartz used to estimate C_{diel}, the expansion of the plasma beyond the electrodes and the presence of parasitic capacitances hinder an accurate determination of C_{diel} using the theoretical coaxial relation [34]. Therefore, in this work, the largest value for ζ_{diel} was determined using pure argon which yields a highly diffuse discharge. This value, hereafter represented by C^{exp}_{diel}, is found to be around 83 pF and is independent of the pressure range of interest. To increase confidence in the determination of C^{exp}_{cell} and ζ_{diel}, both positive and negative half-cycles are fitted and the obtained values averaged, with the exception of the Lissajous curves for the empty reactor at atmospheric pressure. Under these conditions, the asymmetric nature of the discharge hinders fitting the active phase of the negative half-cycle. The displacement current i_{dis} given by Eq. (10) is subtracted from the total current i_{total} to determine the plasma current i_{plasma} and thus the charge Q_{plasma} transferred within a half-cycle, i.e. over a half-period $T/2$ (Eq. (11)). The so-called burning voltage U_b is determined by (12), where ΔU is half of the width of the Lissajous curve at $Q_{total} = 0$ and used to estimate the reduced electric field strength via (13), where $d_{gap} = 4.65\,mm$ is the reactor gap [35, 36]. It should be noted that the reduced electric field strength determined in this fashion provides a spatially and temporally averaged estimation [37] and is used to investigate trends across the different experimental conditions. The determination of local electric fields, which vary within micrometric and nanosecond scales at atmospheric pressure and ultimately determine the plasma chemistry [38], has not been pursued.

$$\beta = \frac{\zeta_{\text{diel}} - C_{\text{cell}}^{\text{exp}}}{C_{\text{diel}}^{\text{exp}} - C_{\text{cell}}^{\text{exp}}} \tag{9}$$

$$i_{\text{dis}} = C_{\text{cell}}^{\text{exp}} \frac{dV_{\text{app}}}{dt} \tag{10}$$

$$Q_{\text{plasma}} = \int_{T/2} i_{\text{plasma}}\, dt \tag{11}$$

$$U_b = \frac{1 - C_{\text{cell}}^{\text{exp}} / C_{\text{diel}}^{\text{exp}}}{1 - C_{\text{cell}}^{\text{exp}} / \zeta_{\text{diel}}^{\text{exp}}} \Delta U \tag{12}$$

$$E/n = \frac{U_b}{d_{\text{gap}} n (1 - \gamma)} \tag{13}$$

Optical Emission Spectroscopy

The light from the discharge is collected using an axially positioned parabolic mirror serving as collimator and coupled into an optical fiber connected to the spectrometer. First, a compact low-resolution spectrometer (Ocean Optics S2000) is used to optimize the mirror position for maximum emission signal using the most intense peak of the Second Positive System (SPS) of N_2^* (337.1 nm) as reference. This step is necessary, because the radial orientation of the optical access openings of the alumina spacers that hold the inner electrode in place (see Fig. 1) may vary after the reactor is disassembled and reasssembled, for example in order to introduce the packing. The actual OES measurements are performed with the high-resolution Echelle spectrometer introduced in Sect. "Experimental" allowing to capture the entire spectral range with one exposure. Since the light intensity emitted by the DBD is relatively weak, especially at atmospheric pressure, exposure times of several minutes are required to record the high-resolution spectra. The recorded spectra are intensity calibrated using an Ulbricht sphere (above 360 nm) and a Deuterium lamp (below 360 nm). The wavelength calibration is performed before the measurement using a Hg lamp and the spectrometer's control software.

An example of a fully calibrated spectrum obtained with the empty reactor at 50 mbar is shown in Fig. 3a. The spectra are largely dominated by N_2 SPS emission at all pressures with and without packing. However, when decreasing the pressure, hydrogen atomic lines, H_α and H_β, as well as the First Negative System of N_2^+ become gradually more intense. As discussed in more detail later, NH^* is not observed in the spectra, except for extremely minor contributions at the lowest investigated pressures, where its intensity is still orders of magnitude weaker than that of N_2^*, as shown in Fig. 3b, where the 50 mbar spectrum is compared to that obtained at 13 mbar. The OES spectra are fitted using the transitions involving $\Delta\nu = -1$ and $\Delta\nu = -2$ bands with the software massiveOES to determine the rotational (T_{rot}) and vibrational (T_{vib}) temperatures of $N_2(C^3\Pi_u)$ [39]. The temperatures typically agree very well and the deviation between the two fits is much lower than the overall uncertainty assigned to the fitting itself. A projection of these temperatures to the ground state $N_2(X^1\Sigma_g^+)$ at the investigated pressures is not trivial. In particular, since

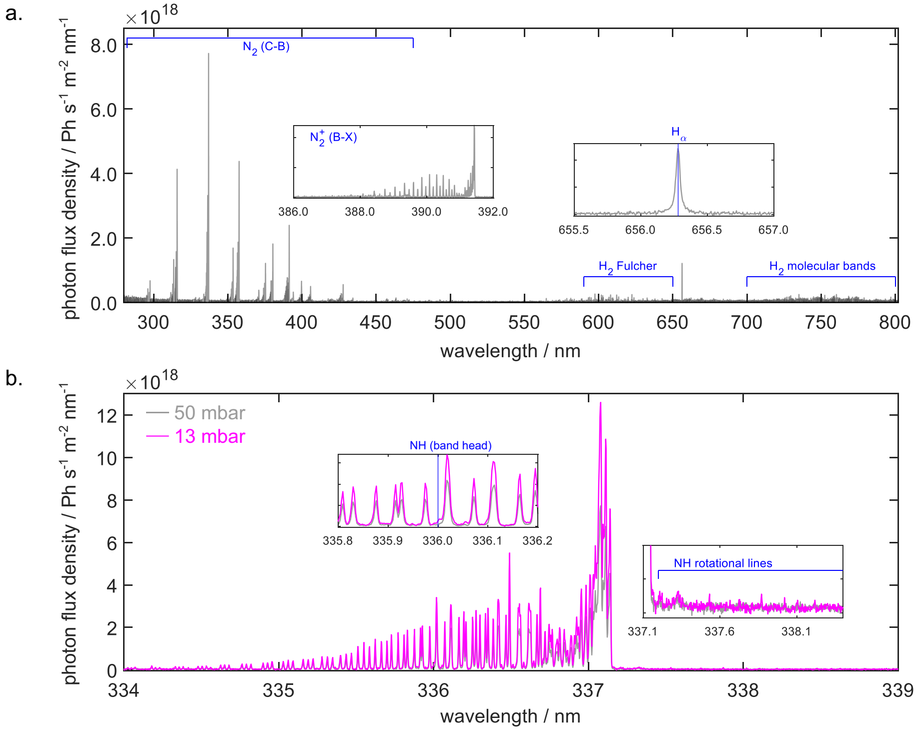

Fig. 3 **a**. Emission spectrum obtained for the empty configuration at 50 mbar, $P_{\mathrm{gen}} = 100\,\mathrm{W}$, $F_{\mathrm{total}} = 100\,\mathrm{sccm}$, $[\mathrm{N_2}] = 25\,\mathrm{vol.\%}$. **b**. zoom-in into $334 - 339\,\mathrm{nm}$, corresponding to the region where the band N_2 (C-B, 0-0) overlaps with the NH(A-X) band. In b. the spectrum obtained at 50 mbar (black line) is compared to that obtained at 13 mbar (magenta line). The insets indicate the excited species responsible for the main features

the lifetimes of N_2(C) in presence of H_2 are estimated to be around 10^{-10} s at 920 mbar (using the data available in [40, 41]) and close to the rotational-translational relaxation times [42], the rotational temperatures of N_2(C) are not necessarily representative of the gas temperature. For this reason, this work reports on T_{rot} and T_{vib} of N_2(C). The emission of N_2^* (330.0 – 338.0 nm), N_2^{+*} (386.0 – 391.9 nm) and H_α (656.1 – 656.5 nm) are integrated to calculate normalized intensity ratios.

Results and Discussion

Effect of Pressure on the Electrical Characteristics

The decrease of pressure in a DBD has a strong effect on the nature of the discharge, both optically as well as in the corresponding current waveforms and Lissajous curves (Fig. 4). With the empty reactor, the discharge is markedly filamentary at 920 mbar and 500 mbar (Fig. 4a and b). At 920 mbar the current waveforms reflect the asymmetric nature of the DBD reactor: high-intensity microdischarges are more prevalent in the negative half-cycle

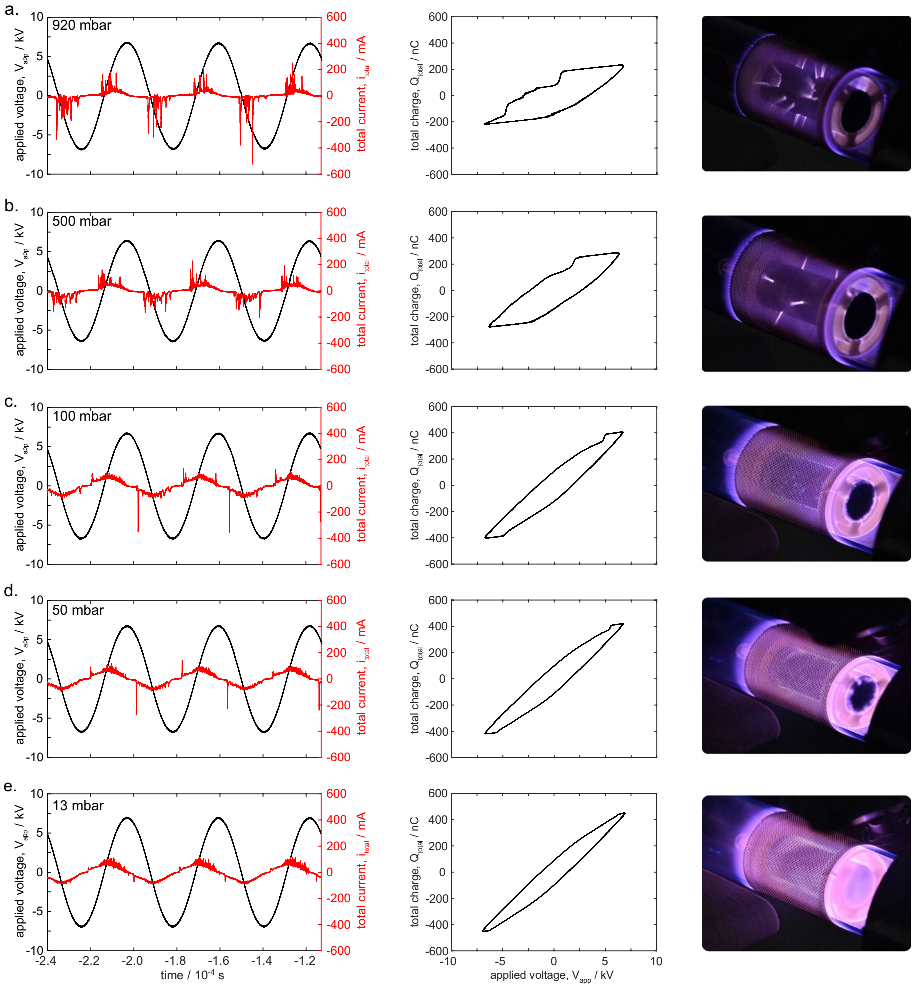

Fig. 4 Applied high-voltage, total current waveforms and Lissajous curves obtained with the empty reactor at **a**. 920 mbar, **b**. 500 mbar, **c**. 100 mbar, **d**. 50 mbar, **e**. 13 mbar using the standard conditions: $P_{\mathrm{gen}} = 100\,\mathrm{W}$, $F_{\mathrm{total}} = 100\,\mathrm{sccm}$, $[\mathrm{N_2}] = 25\,\mathrm{vol.\%}$. The photos were taken with an unpainted quartz tube using the digital camera settings: aperture f/9, shutter speed 1/25, ISO 8000

when the quartz tube acts as the cathode. By reducing the pressure to 500 mbar, the discharge is still filamentary, albeit with a reduction in the intensity of the microdischarges, rendering the waveforms relatively more symmetric.

When decreasing the pressure below 275 mbar, filaments are no longer observed with the naked eye. This is consistent with the findings from Engeling et al., who reported a mode transition in a packed bed reactor, in which air plasma transitions from a regime where filamentary microdischarges dominate to a discharge characterized by surface ionization waves below 266 mbar [43]. At 100 mbar and lower the discharge appears highly diffuse, thereby occupying a large fraction of the gas volume (Fig. 4c to e) which results in an increase in discharge fraction β. The current waveforms exhibit similar positive and negative half-cycles, characterized by low-intensity, high-frequency current spikes super-imposing a larger slowly varying signal. Moreover, a current spike appears at the beginning of the active phases and decreases in intensity when lowering the pressure from 100 to 13 mbar. In this range, for a constant $P_{\text{gen}} = 100\,\text{W}$, the resulting plasma power is found to slightly decrease from $\simeq 49$ W to $\simeq 44$ W with the decrease of pressure. Introducing SiO_2 beads in the discharge volume results in two main effects: (i) an overall reduction of the current peak values of the microdischarges at all pressures, and (ii) a suppression of the filaments (no longer visible) at 500 and 920 mbar. The transition from filamentary microdischarges to surface ionization waves with quartz packing is discussed at length in the modelling work by Engeling et al. [43]. Q_{plasma} and β are mainly affected by pressure and power, with only minor differences between empty and packed configurations.

An important effect arising when reducing the pressure is a gradual extension of the active phase ("plasma ON" time t_{ON}), which can be observed both in the current waveforms and Lissajous curves. The latter become narrower (i.e. ΔU decreases) and vertically enlongated with the decrease of pressure, since more charge has to be transferred for similar coupled powers (i.e. Q_{plasma} increases). As a result, the active phase in respect to the period of the applied high-voltage T, i.e. t_{ON}/T, increases from 0.59 to 0.88 with the empty reactor and from 0.49 to 0.86 with SiO_2 beads upon decreasing p from 920 to 13 mbar. As discussed below in more detail, while a decrease in pressure yields a reduction in ΔU (e.g. $\Delta U \simeq 3.1\,\text{kV}$ at 920 mbar, $\Delta U \simeq 1.3\,\text{kV}$ at 13 mbar), p has a much stronger impact on n, which results in an overall increase of E/n according to p^{-1} (Eq. (13)).

Effect of Pressure on NH_3 Formation

The results obtained for the pressure dependency investigation are displayed in Fig. 5, with the empty symbols representing the empty configuration and filled symbols corresponding to the packed reactor. From 920 to 100 mbar, the concentration of NH_3 remains constant with the empty reactor, while a decrease is observed for the packed configuration. The further decrease of pressure leads to an increase of $[NH_3]$. This effect is enhanced in the packed configuration, with which $[NH_3]$ increases from $\simeq 1230$ to 2530 ppm upon decrease of pressure from 100 to 13 mbar. Such behaviour occurs even though the discharge remains diffuse at these pressures and unaffected by the introduction of beads. The decrease in pressure leads to an increase in β towards values close to 1 (Fig. 5b) and larger transferred charge (Fig. 5c), with similar values for both empty and packed configurations. The energy yield as a function of pressure has the same trend than that displayed in Fig. 5a for $[NH_3]$. For example, the energy yields with packing at 920 and 13 mbar are, respectively, 0.15 and 0.27 g-NH_3 kWh^{-1}. T_{vib} of $N_2(C)$ remains constant at about 3700 K in the whole pressure range and T_{rot} is around 370 K between 13 and 100 mbar and increases to about 480 K at 920 mbar (Fig. 5d). The effect of pressure on the ammonia yield is attributed to the interplay between the residence time and E/n as discussed next.

The decrease in $[NH_3]$ from 920 to 100 mbar with the packed configuration (Fig. 5a) may be attributed to a decrease in the residence time, which is directly proportional to the pressure (Eq. (7)). At 100 mbar both empty and packed configurations yield similar $[NH_3]$. Below 100 mbar, the residence time is further reduced to $\sim$ 10 ms which cannot explain the increase in $[NH_3]$ since production-dominant regimes in DBDs are expected with residence times up to several seconds [44]. Rather, E/n substantially increases in this pressure range

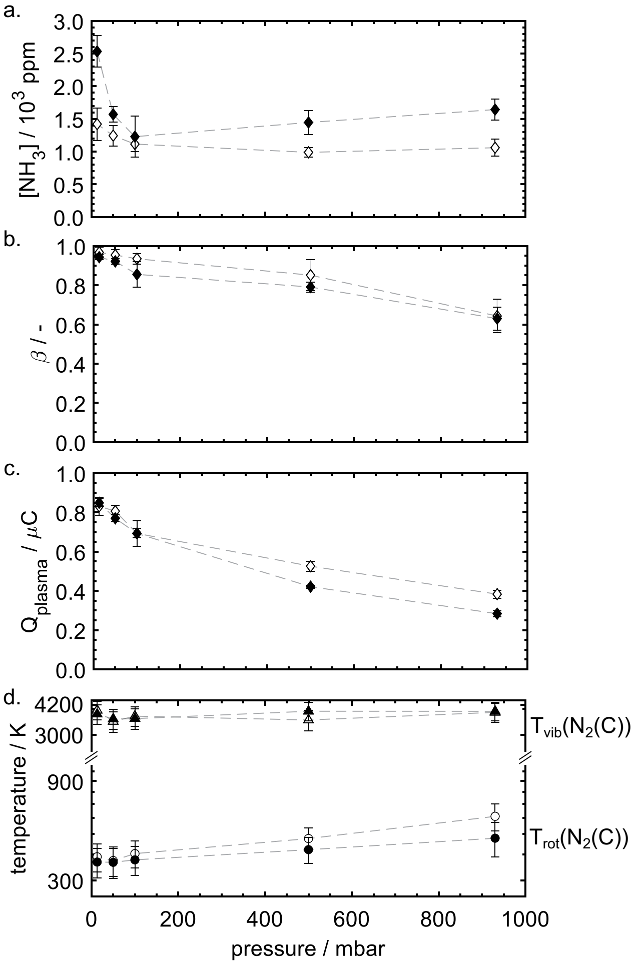

Fig. 5 Results obtained for the pressure scan experiments for $P_{\mathrm{gen}} = 100\,\mathrm{W}$, $F_{\mathrm{total}} = 100\,\mathrm{sccm}$, $[\mathrm{N_2}] = 25\,\mathrm{vol.\%}$. **a**. NH_3 concentration at the outlet, **b**. discharging fraction β, **c**. charge transferred during the active negative half-cycle, **d**. rotational (circles) and vibrational (triangles) temperatures. Empty data points: empty reactor, filled data points: reactor packed with SiO_2

which can be qualitatively compared with the increase of $[NH_3]$ in Fig. 6a and b. Note that the larger *E*/*n* values in Fig. 6b for the packed reactor are due to the effective lower gap (Eq. (13)). Similar reduced electric field strengths have been reported elsewhere with DBDs operated at comparable pressures [45–47]. As discussed in several works, the increase in *E*/*n* leads to more energetic electrons which significantly alter the plasma chemistry in H_2−N_2−NH_3 plasmas [23, 48, 49]. For instance, as discussed by Rouwenhorst et al. [48], in N_2−H_2 $25 - 75\,\mathrm{vol.\%}$ plasmas with a gas temperature of 400 K and a vibrational temperature of 3000 K, vibrational excitation of N_2 in N_2-H_2 dominates at $E/n < 10\,\mathrm{Td}$. Above 200 Td, ionization and dissociation processes of N_2 and H_2 become increasingly important relative to the electronic excitation of N_2. This is in line with the increase of both N_2^+/N_2^* and H_α/N_2^* intensity ratios (normalized to their maximum) between 100 and 13 mbar (Fig. 6c and d),

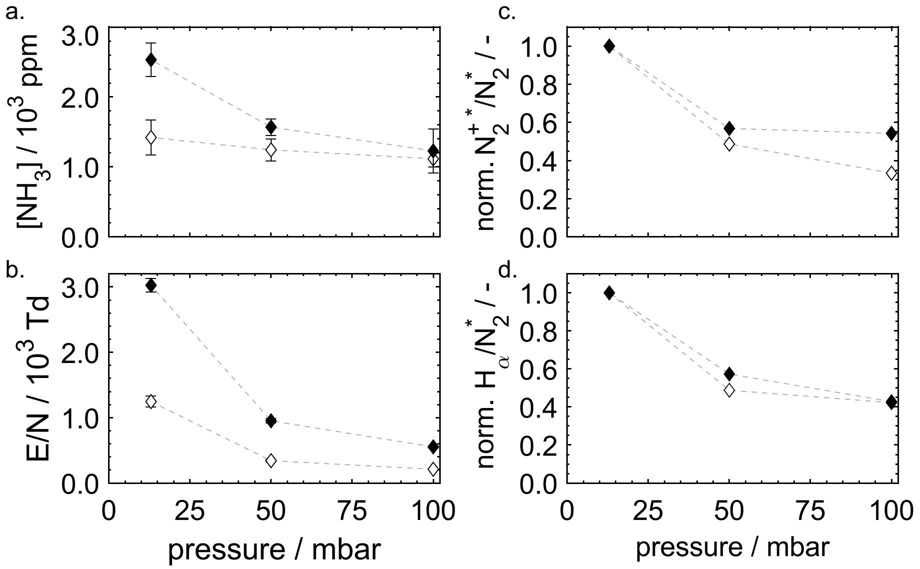

Fig. 6 Results obtained for the pressure scan experiments for $P_{\mathrm{gen}} = 100\,\mathrm{W}$, $F_{\mathrm{total}} = 100\,\mathrm{sccm}$, $[\mathrm{N_2}] = 25\,\mathrm{vol.\%}$. **a**. NH_3 concentration at the outlet, **b**. mean reduced electric field strength determined using Eq. (13), **c**. N_2^{+*}/N_2^* normalized intensity ratio, **d**. H_α/N_2^* normalized intensity ratio. Empty data points: empty reactor, filled data points: reactor packed with SiO_2

which cannot be solely explained by the effect of pressure on the quenching of N_2(C), N_2^+(B) and H_α by H_2 and N_2 (see Sect. "Normalized Intensity Ratios, [NH_3] and *E*/*n*").

Owing to the large *E*/*n* at reduced pressures, the observed increase in [NH_3] is attributed to a larger availability of both atomic H and N by electron-impact dissociation of H_2 and N_2. At the same time, NH_3 electron-impact dissociation is reduced by the absence of microdischarges, which are important ammonia loss channels in a filamentary plasma [19, 20]. Note that the dissociation of NH_3 by collisions with $N_2(A^3)$ metastables, relevant in highly diluted NH_3/N_2 plasmas [23], is expected to be of reduced importance in N_2-H_2 plasmas due to quenching of $N_2(A^3)$ by H and H_2 [6, 50]. The larger availability of atomic species in the plasma volume enables formation of NH_x(s) intermediates through Eley-Rideal reactions in packed configuration, thereby increasing [NH_3]. The interplay between the residence time and reduced electric field strength in the pressure range $100 - 500$ mbar has also been discussed by Sun et al. in nanopulsed DBD N_2-H_2 discharges [46].

The two plasma regimes - filamentary and diffuse - are studied in the next sections for various plasma powers, feed gas compositions and flow rates at two representative pressures: 50 and 920 mbar.

Effect of Plasma Power on NH_3 Formation

Figure 7 shows the effect of plasma power on [NH_3] and electrical characteristics. In general, the increase in power results in larger Q_{plasma} and β, both of which with significantly higher values at 50 mbar. [NH_3] increases with plasma power, in agreement with other literature studies [44, 51–53]. Generally speaking, the increase in power delivered to the

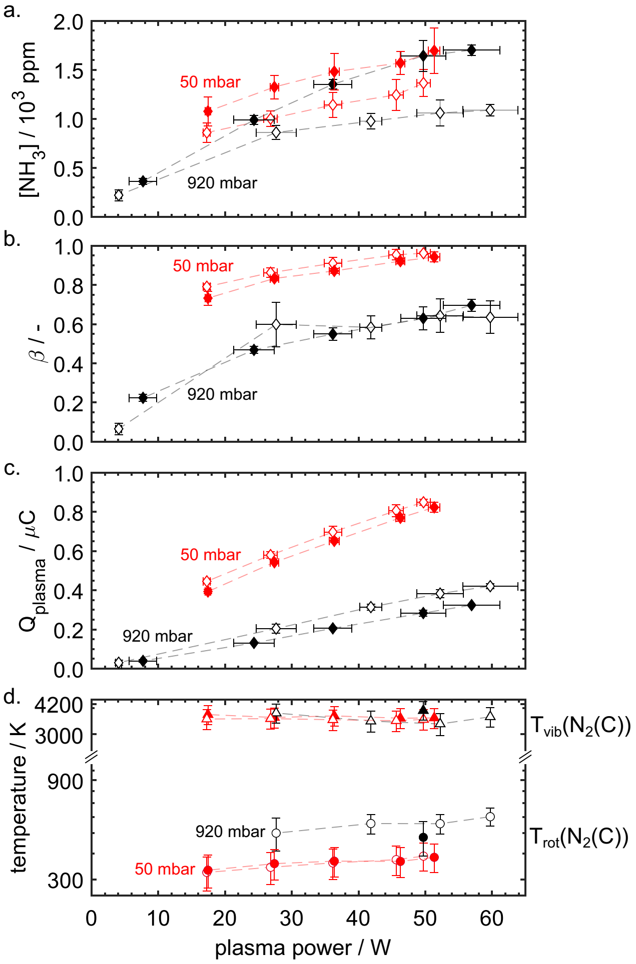

Fig. 7 Results obtained for the power scan experiments for $F_{\text{total}} = 100\,\text{sccm}$, $[N_2] = 25\,\text{vol.\%}$ at 920 and 50 mbar. **a**. NH_3 concentration at the outlet, **b**. discharging fraction β, **c**. charge transferred during the active negative half-cycle, **d**. rotational (circles) and vibrational (triangles) temperatures. Empty data points: empty reactor, filled data points: reactor packed with SiO_2, black color: 920 mbar, red color: 50 mbar

discharge produces more reactive species, such as atomic H and N, which contribute to an increase in ammonia formation [7, 54]. Moreover, the increase in β observed at 50 mbar and for the packed configuration at 920 mbar (Fig. 7b) further benefits NH_3 formation by effectively increasing the discharge volume. T_{vib} is found to be independent of the plasma power and reactor configuration, while a slight increasing trend of T_{rot} with power at 920 mbar and 50 mbar can be appreciated in Fig. 7d.

For the lowest generator power $P_{\text{gen}} = 40\,\text{W}$, the resulting plasma power at 920 mbar ($\simeq 4 - 8\,\text{W}$) is significantly lower than at 50 mbar ($\simeq 17\,\text{W}$). The low plasma powers at 920 mbar, and accordingly low β, lead to a significant drop in ammonia synthesis, e.g. down to $\simeq 360\,\text{ppm}$ with the packed configuration (Fig. 7a). In contrast, the greater *E*/*n* at

50 mbar allows a discharge to be sustained with relatively high β, which contributes to a higher plasma power and therefore a larger [NH_3], e.g. $\simeq 1080\,\mathrm{ppm}$ with beads.

For both 920 and 50 mbar the introduction of SiO_2 beads results in larger ammonia concentrations. However, the impact is more pronounced at 920 mbar, especially beyond 30 W. In part, this can be attributed to the relatively constant β with the empty reactor, which implies that the discharge fraction in filamentary mode remains unaffected by the plasma power, thereby limiting the increase in [NH_3]. Also, the electron density in the filaments is expected to rise with the increase of power [55], which contributes to a larger destruction of NH_3 by electron-impact dissociation. In contrast, the SiO_2 beads enable an increase in [NH_3] since they suppress filaments/microdischarges and permit the increase of β with larger powers. Moreover, the beads promote plasma-surface pathways to form NH_3 (e.g. through Eley-Rideal reactions between radicals and adsorbed species) as well as electric field strength enhancement at contact points [43, 56]. At 50 mbar the discharge remains similarly diffuse in both configurations with comparable electrical characteristics, which makes the effect of packing on ammonia formation less pronounced. For both configurations at this pressure, an increase in plasma power yields larger plasma volumes (i.e. β increases), hence enabling larger ammonia concentrations.

Effect of the Inlet Concentration on NH_3 Formation

The effect of feed gas composition on NH_3 formation and plasma characteristics is shown in Fig. 8 for a constant total feed flow rate and generator power at 920 and 50 mbar. Under these conditions, β and Q_{plasma} are found to be independent of [N_2] and therefore not shown. With the empty reactor at 920 mbar, [NH_3] remains constant for 10 and 25 vol.% N_2 and decreases monotonically from 25 to 75 vol.% N_2. Packing the reactor favours NH_3 synthesis across the whole [N_2] range, with the largest enhancement at 40 vol.% N_2: [NH_3

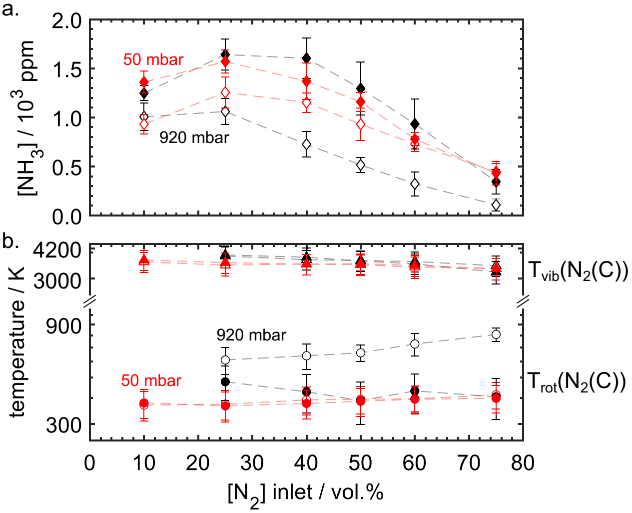

Fig. 8 Results obtained for the feed concentration scan experiments for $P_{\mathrm{gen}} = 100\,\mathrm{W}$, $F_{\mathrm{total}} = 100\,\mathrm{sccm}$ at 920 and 50 mbar. **a**. NH_3 concentration at the outlet, **b**. rotational (circles) and vibrational (triangles) temperatures. Empty data points: empty reactor, filled data points: reactor packed with SiO_2, black color: 920 mbar, red color: 50 mbar

] increases from $\simeq 726$ ppm to $\simeq 1603$ ppm with SiO_2 beads, resulting in a shift of the maximum towards larger [N_2], which means that lower amounts of hydrogen are required to produce similar quantities of [NH_3]. This shift is attributed to the lower dissociation energy of H_2 compared to N_2, which results in adsorbed H(s) being the main adsorbate on the packing's surface according to Andersen et al. [44]. Saturating the surface with H(s) inhibits adsorption of other important plasma-phase species, and as a result a larger amount of N_2 is required to increase the likelihood of atomic N adsorbing on the surface and enable formation of NH_x(s) precursors [57, 58]. The variation in the optimum gas composition in DBDs depending on the physical and chemical properties of the packing materials has been reported in the literature [13, 52, 59].

At 50 mbar there is a significant improvement in [NH_3] between 40−75 vol.% N_2 without beads. This is attributed to the absence of filaments as well as to the larger *E*/*n* favouring N_2 dissociation into N. Although with the introduction of beads there is a further increase in [NH_3] due to plasma-surface reactions, the benefit of using beads in this concentration range is significantly more limited than at 920 mbar. Another aspect seldom discussed in the literature is the impact of the N_2−H_2 gas composition on the vibrational and rotational temperatures (Fig. 8b). At 920 mbar and with empty reactor, T_{vib} decreases from 3850 to 3460 K, while T_{rot} increases from 609 to 808 K for 25−75 vol.% N_2. In presence of beads, there is a sharp reduction in the rotational temperatures down to ≈ 400 K over the whole concentration range, close to the values obtained at 50 mbar and to the background gas temperatures measured with the thermocouple.

Effect of the Feed Flow Rate on NH_3 Formation

Decreasing the feed flow rate from 300 to 25 sccm leads to an increase in [NH_3] shown in Fig. 9a, while the electrical properties of the plasma (not shown) as well as the rotational and vibrational temperatures (Fig. 9b.) remain constant. With the decrease of the feed flow rate, both the specific energy input and residence time increase 12-fold (Eqs. (6) and (7)). The [NH_3] concentration shown in Fig. 9a is plotted as function of the effective residence time $\tau^{\mathrm{eff}}_{\mathrm{plasma}}$ and SEI in Fig. 10 (note the log scale in the *x*-axis of the residence time plot), with $\tau^{\mathrm{eff}}_{\mathrm{plasma}} = \tau_{\mathrm{plasma}}(t_{\mathrm{ON}}/T)\beta$ to account for a longer plasma exposure at lower pressures. Generally put, an increase in residence time increases the likelihood of radicals to undergo plasma-surface reactions, while a large SEI is conducive to more energy being transferred into the plasma, thereby promoting dissociation of H_2 and N_2. Although the increase in residence time and specific energy input also promotes dissociation of NH_3 in ammonia plasmas [19], the increase of [NH_3] with both $\tau^{\mathrm{eff}}_{\mathrm{plasma}}$ and SEI in Fig. 10 demonstrates that the discharge is in a production-dominated regime. With 25 sccm the increase in [NH_3] with packing is substantial at 920 mbar while no effect is observed at 50 mbar. This is explained by the discharge modification induced by the introduction of SiO_2 beads at 920 mbar and the longer residence times at this pressure.

Absence of NH(A-X) Emission

Excited $NH^*(A^3\Pi \rightarrow X^3\Sigma^-)$ with most intense emission at 336.0 nm, reported in other works with N_2-H_2 DBD discharges (see e.g. [60, 61]) and whose formation has been pro-

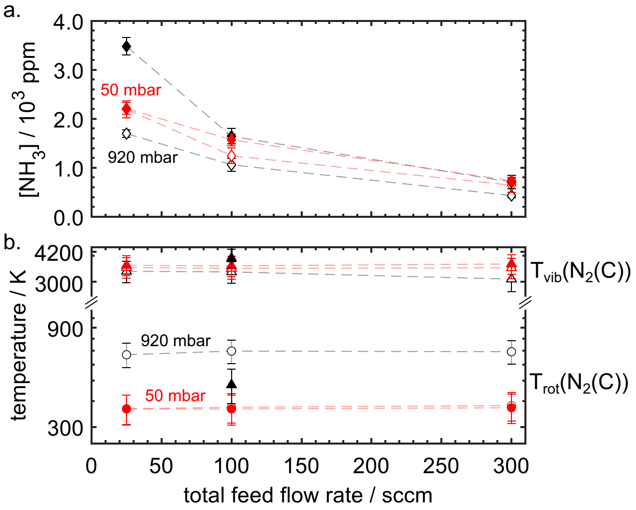

Fig. 9 Results obtained for the total feed flow scan experiments for $P_{gen} = 100\,W$, $[N_2] = 25\,vol.\%$ at 920 and 50 mbar. **a**. NH_3 concentration at the outlet, **b**. rotational (circles) and vibrational (triangles) temperatures. Empty data points: empty reactor, filled data points: reactor packed with SiO_2, black color: 920 mbar, red color: 50 mbar

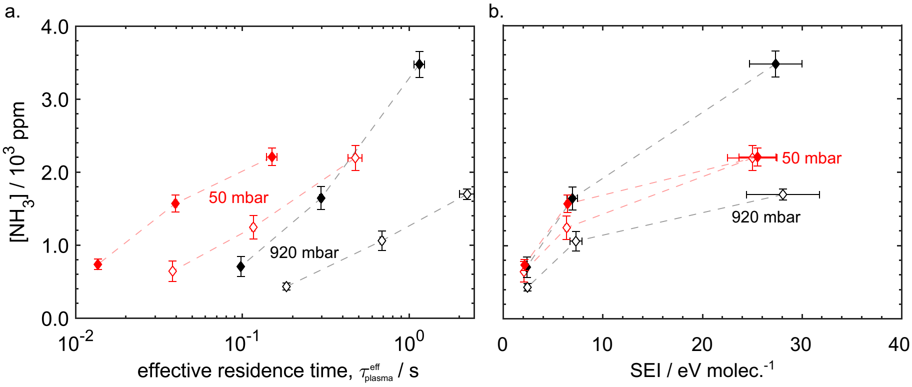

Fig. 10 NH_3 concentration at the outlet as a function of the **a**. effective residence time and **b**. specific energy input, obtained for the the total feed flow rate scan experiments displayed in Fig. 9. Empty data points: empty reactor, filled data points: reactor packed with SiO_2, black color: 920 mbar, red color: 50 mbar

posed as one possible rate-limiting step in ammonia synthesis [62], has not been detected under the investigated conditions, both in empty configuration as well as with the reactor packed with SiO_2 beads. These studies have used relatively low resolution spectrometers, with which NH^* is identified in the shoulder of the N_2 (C-B, 0-0) band. As shown in Fig. 3b, this band consists of many rotational features, which are not distinguishable in low resolution spectra. Under the experimental conditions pursued in this work, no distinct peak at 336.0 nm can be discerned, which is in agreement with the findings reported by

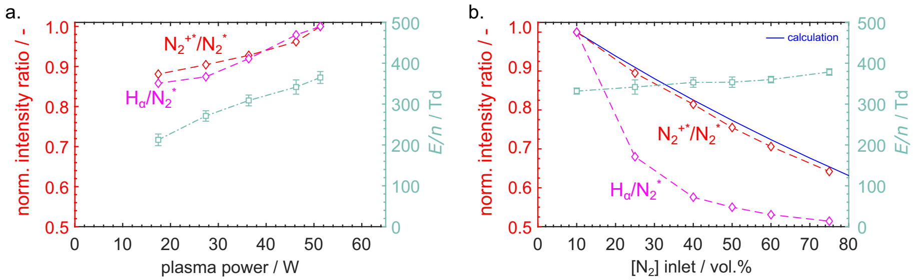

Fig. 11 Normalized intensity ratios (diamond symbols; red: N_2^{+*}/N_2^*, magenta: H_α/N_2^*) and mean reduced electric field strengths determined using Eq. (13) (square symbols) as a function of **a**. plasma power and **b**. N_2 concentration, for the empty reactor at 50 mbar. The calculated N_2^{+*}/N_2^* normalized intensity ratio estimated using depopulation rates for the concentration scan is plotted as solid blue line

Chen et al. [30]. Since the threshold for the electronic transition from the ground state to NH(A) is only around 3.7 eV [63], these observations suggest that either NH(X) is not present in sufficient quantities in the gas phase and/or the excited state NH(A) is effectively quenched by H_2 [64]. Modelling work by van't Veer et al. predicts that the number densities of NH produced in microdischarges are close to that of atomic N and several orders of magnitude lower than H [57].

Normalized Intensity Ratios, [NH_3] and *E*/*n*

Several studies have correlated intensity ratios of excited species in N_2-H_2 DBD plasmas with ammonia synthesis rates, sometimes with conflicting conclusions. For example, Wang et al. correlated an increase in NH_3 synthesis with the increase of N_2^{+*}/N_2^* and H_α/N_2^* when packing the DBD with Ni/γ-Al_2O_3 beads, an effect explained by the larger availability of radicals in the plasma [7]. Instead, Patil et al. established a link between a decrease of [NH_3] with Mn/γ-Al_2O_3 beads and a higher N_2^{+*}/N_2^*, attributed to a less efficient use of the electron energy into ionization of N_2 [52]. While a necessary condition that allows this to be done is to use intensity-calibrated spectrometers, several factors can contribute to the observed intensity ratios, as discussed below.

In Sect. "Effect of Pressure on NH_3 Formation", the increase in [NH_3] with the decrease of pressure from 100 to 13 mbar is correlated with an increase in *E*/*n*. The resulting larger electron energies at lower pressures contribute to an in increase in both N_2^{+*}/N_2^* and H_α/N_2^* normalized intensity ratios. A similar comparison can be done for the dependency with the plasma power, e.g. for the empty reactor at 50 mbar: [NH_3] is found to increase with the plasma power (Fig. 7a), which can also be used to explain the observed increase in *E*/*n* as well as N_2^{+*}/N_2^* and H_α/N_2^* (Fig. 11a). Note that the N_2^{+*}/N_2^* intensity ratio is widely used in the literature to estimate *E*/*n* in air or pure N_2 plasmas [65]. Such a method requires the development of detailed kinetic models that compute population and depopulation of excited levels as well as dedicated calibration procedures, which are beyond the scope of this work [66, 67].

The correlations between [NH_3], *E*/*n* and intensity ratios cannot be so easily established for the dependency with [N_2]. As discussed in Sect. "Effect of the Inlet Concentration on NH_3 Formation", [NH_3] decreases between 25 and 75 vol.% [N_2], e.g. for the empty reactor at 50 mbar. The N_2^{+*}/N_2^* and H_α/N_2^* normalized intensity ratios also decrease with [N_2], but differently from one another as displayed in (Fig. 11b), suggesting additional factors influencing the emission of the excited states. Under these conditions, *E*/*n*, which even slightly increases with [N_2], is no longer a good representation of N_2^{+*}/N_2^*. Instead, the decrease of N_2^{+*}/N_2^* with [N_2] can be well explained by the role played by H_2 and N_2 on the quenching of the excited states, which can be demonstrated by considering their influence on the lifetimes of $N_2(C^3\Pi_u)_{\nu=0}$ and $N_2^+(B^2\Pi_u^+)_{\nu'=0}$, hereafter labeled as C and B states, respectively. The lifetimes afftect the intensity ratio I_B/I_C given by (14), where $\tau_0^{B/C}$ are the natural lifetimes ($\tau_0^B = 62.3\,\mathrm{ns}$ [68], $\tau_0^C = 42\,\mathrm{ns}$ [40]) and $\tau_{\mathrm{eff}}^{B/C}$ are the effective lifetimes determined by (15) [69]. $k_{q,N_2}^B = 8.84\times10^{-10}\,\mathrm{cm^3\,s^{-1}}$ [70], $k_{q,N_2}^C = 0.13\times10^{-10}\,\mathrm{cm^3\,s^{-1}}$ [40], $k_{q,H_2}^B = 6.8\times10^{-10}\,\mathrm{cm^3\,s^{-1}}$ and $k_{q,H_2}^C = 3.2\times10^{-10}\,\mathrm{cm^3\,s^{-1}}$ [41] are the depopulation rates of the corresponding energy levels by collision with N_2 and H_2, and n_{N_2} and n_{H_2} are the number densities of N_2 and H_2 determined at 50 mbar and 373 K using the ideal gas law. Note that the full expression for I_B/I_C also includes the reaction rates for the electron excitation from the ground state which depend on *E*/*n* [71]. However, since *E*/*n* is weakly dependent on [N_2] and only a comparison with normalized intensity ratios is pursued, they are not considered.

$$\frac{I_B}{I_C} \sim \frac{\tau_0^C \tau_{\mathrm{eff}}^B}{\tau_0^B \tau_{\mathrm{eff}}^C} \tag{14}$$

$$\frac{1}{\tau_{\mathrm{eff}}^{B/C}} = \frac{1}{\tau_0^{B/C}} + k_{q,N_2}^{B/C} n_{N_2} + k_{q,H_2}^{B/C} n_{H_2} \tag{15}$$

The I_B/I_C normalized to its maximum value is plotted in blue in Fig. 11b with a very good agreement with the normalized intensity ratios obtained with OES. This is a strong indication that the light emitted by N_2^+(B-X) and N_2(C-B) transitions at different gas compositions is mainly governed by H_2 and N_2 quenching. A similar approach using the effective lifetime for H_α and quenching rates by H_2 and N_2 available in the literature [72] does not explain the observed trend for H_α/N_2^* in Fig. 11b, indicating the need for more sophisticated approaches, such as collisional radiative models [73]. This discussion, which becomes even less trivial when the plasma is in contact with materials with given physical-chemical properties, demonstrates that establishing a link between the emission of excited species with [NH_3] and *E*/*n* should be done with caution.

Conclusions

The influence of a wide pressure range on the electrical characteristics, optical emission and NH_3 formation in a coaxial DBD is presented. At pressures above 275 mbar the discharge is characterized by filaments/microdischarges, while for lower pressures the plasma becomes diffuse with a large volume occupation. Introducing SiO_2 beads in the discharge volume at 920 mbar induces a strong suppresion of filaments or intense microdischarges. The suppression of filaments alongside the presence of plasma-surface pathways to form NH_3 are important factors enabling larger [NH_3] in presence of beads. At pressures $\leq 100\,\mathrm{mbar}$, the

SiO_2 beads have a minor impact on the discharge morphology and discharge fraction (β). However, decreasing the pressure from 100 to 13 mbar favours ammonia formation, especially in the presence of beads. This is attributed to the increase of E/n, which favours the production of atomic species, alongside plasma-surface reactions enabled by the SiO_2 beads (e.g. Eley-Rideal), resulting in an overall increase of $[NH_3]$.

Under the studied conditions, the main transitions identified in the emission spectra are N_2(C-B), N_2^+(B-X), H_α and H_2 molecular bands, with no differences for both reactor configurations. The rotational temperature of N_2(C) at 920 mbar decreases in presence of beads, an effect which enhanced towards larger concentrations of $[N_2]$ in $[H_2]$, while the vibrational temperatures are found to be in the range of $3500 - 3900$ K. The normalized intensity ratios of N_2^+/N_2^* and H_α/N_2^* are found to increase below 100 mbar, indicating the increasing importance of ionization and dissociation processes. Excited NH^* has not been identified in the emission spectra, evidencing that NH(X) is either not present in sufficient amounts in the plasma volume or NH(A) is effectively quenched e.g. by H or H_2. These findings shall be used to benchmark N_2-H_2 kinetic models.

The role played by NH on NH_3 synthesis could not be confirmed in this study and the limitations in correlating intensity ratios with synthesis rates have been addressed. These findings underscore the importance of a systematic and careful use of spectroscopic techniques in the literature of DBDs packed with dielectrics and catalyst materials in order to ellucidate the impact of their physical and chemical characteristics on the plasma properties and NH_3 formation.

Acknowledgements The authors are thankful for the fruitful discussions with Vinzenz Wolf and Dr. Roland Friedl.

Author Contributions R.A. and A.M. conceptualized and designed the work. R.A. and A.M. carried out the experimental work and formal data analysis. R.A. wrote the original draft. R.A., A.M., A.H. and U.F. reviewed and edited the manuscript.

Funding Open Access funding enabled and organized by Projekt DEAL. The authors declare they received no funding to pursue this work.

Data Availability The authors declare that the data supporting the findings of this study are available within the paper.

Declarations

Competing interests The authors declare no competing interests.

References

1. Jauberteau JL, Jauberteau I, Aubreton J (2002) J Phys D Appl Phys 35:665–74. https://doi.org/10.1088/0022-3727/35/7/315
2. Uyama H, Matsumoto O (1989) Plasma Chem Plasma Process 9:421–32. https://doi.org/10.1007/BF01083676
3. Antunes R, Steiner R, Romero Muñiz C, Soni K, Marot L, Meyer E (2021) ACS Appl Energy Mater 4:4385–94. https://doi.org/10.1021/acsaem.0c03217
4. Shah J, Wang W, Bogaerts A, Carreon ML (2018) ACS Appl Energy Mater 1:4824–39. https://doi.org/10.1021/acsaem.8b00898
5. de Castro A, Alegre D, Tabarés F (2015) J Nucl Mater 463:676–9. https://doi.org/10.1016/j.jnucmat.2014.12.038
6. Chatain A, Morillo-Candas AS, Vettier L, Carrasco N, Cernogora G, Guaitella O (2023) Plasma Sources Sci Technol 32:035002. https://doi.org/10.1088/1361-6595/acc132
7. Wang Y, Craven M, Yu X, Ding J, Bryant P, Huang J, Tu X (2019) ACS Catal 9:10780–93. https://doi.org/10.1021/acscatal.9b02538
8. Gorbanev Y, Engelmann Y, van't Veer K, Vlasov E, Ndayirinde C, Yi Y, Bals S, Bogaerts A (2021) Catalysts 11:1230. https://doi.org/10.3390/catal11101230
9. Vervloedt SCL, von Keudell A (2024) Plasma Sources Sci Technol 33:045005. https://doi.org/10.1088/1361-6595/ad38d6
10. Humphreys J, Lan R, Tao S (2020) Adv Energy Sustain Res 2. https://doi.org/10.1002/aesr.202000043
11. Ben Yaala M, Scherrer DF, Saeedi A, Moser L, Soni K, Steiner R, De Temmerman G, Oberkofler M, Marot L, Meyer E (2020) Nucl Fusion 60:016026. https://doi.org/10.1088/1741-4326/ab519c
12. Zhu X, Hu X, Wu X, Cai Y, Zhang H, Tu X (2020) J Phys D Appl Phys 53:164002. https://doi.org/10.1088/1361-6463/ab6cd1
13. Ndayirinde C, Gorbanev Y, Ciocarlan RG, De Meyer R, Smets A, Vlasov E, Bals S, Cool P, Bogaerts A (2023) Catal Today 419:114156. https://doi.org/10.1016/j.cattod.2023.114156
14. Gorky F, Nambo A, Carreon MA, Carreon ML (2023) Plasma Chem Plasma Process 44:1357–68. https://doi.org/10.1007/s11090-023-10397-w
15. Mehta P, Barboun P, Herrera FA, Kim J, Rumbach P, Go DB, Hicks JC, Schneider WF (2018) Nat Catal 1:269–75. https://doi.org/10.1038/s41929-018-0045-1
16. Antunes R, Marot L, Romero-Muñiz C, Steiner R, Meyer E (2021) Nucl Fusion 61:126046. https://doi.org/10.1088/1741-4326/ac33c6
17. Engelmann Y, van 't Veer K, Gorbanev Y, Neyts EC, Schneider WF, Bogaerts A (2021) ACS Sustain Chem Eng 9:13151–63. https://doi.org/10.1021/acssuschemeng.1c02713
18. Bayer BN, Raskar S, Adamovich IV, Bruggeman PJ, Bhan A (2023) Plasma Sources Sci Technol 32:125005. https://doi.org/10.1088/1361-6595/ad10f0
19. Andersen J, van 't Veer K, Christensen J, Østberg M, Bogaerts A, Jensen A (2023) Chem Eng Sci 271:118550. https://doi.org/10.1016/j.ces.2023.118550
20. Sode M, Jacob W, Schwarz-Selinger T, Kersten H (2015) J Appl Phys. https://doi.org/10.1063/1.4913623
21. Carrasco E, Jiménez-Redondo M, Tanarro I, Herrero VJ (2011) Phys Chem Chem Phys 13:19561. https://doi.org/10.1039/c1cp22284h
22. Jiménez-Redondo M, Chatain A, Guaitella O, Cernogora G, Carrasco N, Alves LL, Marques L (2020) Plasma Sources Sci Technol 29:085023. https://doi.org/10.1088/1361-6595/ab9b1b
23. Bang S, Snoeckx R, Cha MS (2023) J Phys Chem A 127:1271–82. https://doi.org/10.1021/acs.jpca.2c06919
24. Fedirchyk I, Tsonev I, Quiroz Marnef R, Bogaerts A (2024) Chem Eng J 499:155946. https://doi.org/10.1016/j.cej.2024.155946
25. Antunes R, Meindl A, Kranig C, Hecimovic A, Fantz U (2025) Int J Hydrogen Energy 170:151121. https://doi.org/10.1016/j.ijhydene.2025.151121
26. Bogaerts A, Centi G, Hessel V, Rebrov E (2025) Chem Cat Chem. https://doi.org/10.1002/cctc.202401938
27. De Meyer R, Gorbanev Y, Ciocarlan RG, Cool P, Bals S, Bogaerts A (2024) Chem Eng J 488:150838. https://doi.org/10.1016/j.cej.2024.150838
28. Van Turnhout J, Rouwenhorst K, Lefferts L, Bogaerts A (2025) EES Catalysis 3:669–93. https://doi.org/10.1039/d5ey00027k
29. Gómez-Ramírez A, Cotrino J, Lambert RM, González-Elipe AR (2015) Plasma Sources Sci Technol 24:065011. https://doi.org/10.1088/0963-0252/24/6/065011
30. Chen Z, Jaiswal S, Diallo A, Sundaresan S, Koel BE (2022) J Phys Chem A 126:8741–52. https://doi.org/10.1021/acs.jpca.2c05023

31. Hecimovic A, D’Isa F, Carbone E, Drenik A, Fantz U (2020) Rev Sci Instrum 91:113501. https://doi.org/10.1063/5.0013413
32. Hegemann D, Navascués P, Snoeckx R (2025) Int J Hydrogen Energy 100:548–55. https://doi.org/10.1016/j.ijhydene.2024.12.351
33. Peeters FJJ, van de Sanden MCM (2014) Plasma Sources Sci Technol 24:015016. https://doi.org/10.1088/0963-0252/24/1/015016
34. Rad RH, Brüser V, Brandenburg R (2024) Plasma Sources Sci Technol 33:025027. https://doi.org/10.1088/1361-6595/ad27ed
35. Butterworth T, Elder R, Allen R (2016) Chem Eng J 293:55–67. https://doi.org/10.1016/j.cej.2016.02.047
36. Ma Y, Wang Y, Harding J, Tu X (2021) Plasma Sources Sci Technol 30:105002. https://doi.org/10.1088/1361-6595/ac2412
37. Brandenburg R (2017) Plasma Sources Sci Technol 26:053001. https://doi.org/10.1088/1361-6595/aa6426
38. Kogelheide F, Offerhaus B, Bibinov N, Krajinski P, Schücke L, Schulze J, Stapelmann K, Awakowicz P (2019) Plasma Processes Polym. https://doi.org/10.1002/ppap.201900126
39. Voráč J, Synek P, Potočňáková L, Hnilica J, Kudrle V (2017) Plasma Sources Sci Technol 26:025010. https://doi.org/10.1088/1361-6595/aa51f0
40. Pancheshnyi S, Starikovskaia S, Starikovskii A (2000) Chem Phys 262:349–57. https://doi.org/10.1016/s0301-0104(00)00338-4
41. Pancheshnyi S, Starikovskaia S, Starikovskii A (1998) Chem Phys Lett 294:523–7. https://doi.org/10.1016/s0009-2614(98)00879-3
42. Bruggeman PJ, Sadeghi N, Schram DC, Linss V (2014) Plasma Sources Sci Technol 23:023001. https://doi.org/10.1088/0963-0252/23/2/023001
43. Engeling KW, Kruszelnicki J, Kushner MJ, Foster JE (2018) Plasma Sources Sci Technol 27:085002. https://doi.org/10.1088/1361-6595/aad2c5
44. Andersen J, Holm M, van ’t Veer K, Christensen J, Østberg M, Bogaerts A, Jensen A (2023) Chem Eng J 457:141294. https://doi.org/10.1016/j.cej.2023.141294
45. Brandenburg R, Schiorlin M, Schmidt M, Höft H, Pipa AV, Brüser V (2023) Plasma 6:162–80. https://doi.org/10.3390/plasma6010013
46. Sun J, Chen Q, Zhao X, Lin H, Qin W (2022) Plasma Sources Sci Technol 31:094009. https://doi.org/10.1088/1361-6595/ac8e2c
47. Cvetanovič N, Ivkovič SS, Obradovič BM, Kuraica MM (2017) Eur Phys J D. https://doi.org/10.1140/epjd/e2017-80339-7
48. Rouwenhorst KHR, Engelmann Y, van ‘t Veer K, Postma RS, Bogaerts A, Lefferts L (2020) Green Chem 22:6258–87. https://doi.org/10.1039/d0gc02058c
49. Hong J, Pancheshnyi S, Tam E, Lowke JJ, Prawer S, Murphy AB (2018) J Phys D Appl Phys 51:109501. https://doi.org/10.1088/1361-6463/aaa988
50. Yang X, Jans E, Richards C, Raskar S, van den Bekerom D, Wu K, Adamovich IV (2022) Plasma Sources Sci Technol 31:015017. https://doi.org/10.1088/1361-6595/ac3053
51. Akay G, Zhang K (2017) Ind Eng Chem Res 56:457–68. https://doi.org/10.1021/acs.iecr.6b02053
52. Patil BS, Cherkasov N, Srinath NV, Lang J, Ibhadon AO, Wang Q, Hessel V (2021) Catal Today 362:2–10. https://doi.org/10.1016/j.cattod.2020.06.074
53. Zhou G, Zhao H, Wang X, Wang Z, Zhang Y, Zhao X, Chen Q, Chen T, Huang Z, Lin H (2024) Int J Hydrogen Energy 60:802–13. https://doi.org/10.1016/j.ijhydene.2024.02.200
54. Wang X, Du X, Chen K, Zheng Z, Liu Y, Shen X, Hu C (2023) ACS Sustain Chem Eng 11:4543–54. https://doi.org/10.1021/acssuschemeng.2c04715
55. Kim JH, Choi YH, Hwang YS (2006) Phys Plasmas. https://doi.org/10.1063/1.2338282
56. Van Laer K, Bogaerts A (2015) Plasma Sources Sci Technol 25:015002. https://doi.org/10.1088/0963-0252/25/1/015002
57. van ‘t Veer K, Engelmann Y, Reniers F, Bogaerts A (2020) J Phys Chem C 124:22871–22883. https://doi.org/10.1021/acs.jpcc.0c05110
58. van Raak T, Li S, Gallucci F (2023) Chem Eng J 455:140691. https://doi.org/10.1016/j.cej.2022.140691
59. Kim H, Teramoto Y, Ogata A, Takagi H, Nanba T (2016) Plasma Processes Polym. https://doi.org/10.1002/ppap.201600157
60. Liu J, Zhu X, Hu X, Zhang F, Tu X (2022) Vacuum 197:110786. https://doi.org/10.1016/j.vacuum.2021.110786
61. Gorky F, Storr V, Jasinski JB, Carreon ML (2025) ACS Materials Au 5:385–96. https://doi.org/10.1021/acsmaterialsau.4c00159
62. Navascués P, Garrido-García J, Cotrino J, González-Elipe AR, Gómez-Ramírez A (2023) ACS Sustain Chem Eng 1:3621–32. https://doi.org/10.1021/acssuschemeng.2c05877
63. Petitjean L, Ricard A (1984) J Phys D Appl Phys 17:919–29. https://doi.org/10.1088/0022-3727/17/5/008

64. Kawasaki M, Hirata Y, Tanaka I (1973) J Chem Phys 59:648–53. https://doi.org/10.1063/1.1680071
65. Bruggeman P, Brandenburg R (2013) J Phys D Appl Phys 46:464001. https://doi.org/10.1088/0022-3727/46/46/464001
66. Paris P, Aints M, Valk F, Plank T, Haljaste A, Kozlov KV, Wagner HE (2005) J Phys D Appl Phys 38:3894–9. https://doi.org/10.1088/0022-3727/38/21/010
67. Bílek P, Šimek M, Bonaventura Z (2019) Plasma Sources Sci Technol 28:115011. https://doi.org/10.1088/1361-6595/ab3936
68. Gilmore FR, Laher RR, Espy PJ (1992) J Phys Chem Ref Data 21:1005–107. https://doi.org/10.1063/1.555910
69. Šimek M (2014) J Phys D Appl Phys 47:463001. https://doi.org/10.1088/0022-3727/47/46/463001
70. Dilecce G, Ambrico PF, De Benedictis S (2010) J Phys D Appl Phys 43:195201. https://doi.org/10.1088/0022-3727/43/19/195201
71. Kozlov KV, Wagner HE, Brandenburg R, Michel P (2001) J Phys D Appl Phys 34:3164–76. https://doi.org/10.1088/0022-3727/34/21/309
72. Bittner J, Kohse-höinghaus K, Meier U, Just T (1988) Chem Phys Lett 143:571–6. https://doi.org/10.1016/0009-2614(88)87068-4
73. Wünderlich D, Fantz U (2016) Atoms 4:26. https://doi.org/10.3390/atoms4040026